arXiv:cond-mat/0403050v2 [cond-mat.str-el] 10 Mar 2004

# Pair-distribution functions of the two-dimensional electron gas

Paola Gori-Giorgi,* Saverio Moroni, and Giovanni B. Bachelet
*INFM Center for Statistical Mechanics and Complexity and Dipartimento di Fisica, Università di Roma "La Sapienza", Piazzale A. Moro 2, 00185 Rome, Italy*
(Dated: March 22, 2022)

Based on its known exact properties and a new set of extensive fixed-node reptation quantum Monte Carlo simulations (both with and without backflow correlations, which in this case turn out to yield negligible improvements), we propose a new analytical representation of (i) the spin-summed pair-distribution function and (ii) the spin-resolved potential energy of the ideal two-dimensional interacting electron gas for a wide range of electron densities and spin polarization, plus (iii) the spin-resolved pair-distribution function of the unpolarized gas. These formulae provide an accurate reference for quantities previously not available in analytic form, and may be relevant to semiconductor heterostructures, metal-insulator transitions and quantum dots both directly, in terms of phase diagram and spin susceptibility, and indirectly, as key ingredients for the construction of new two-dimensional spin density functionals, beyond the local approximation.

## I. INTRODUCTION AND MAIN RESULTS

The two-dimensional electron gas (2DEG), realized in semiconductor heterostructures, has been a source of lasting inspiration for at least two generations of fundamental and applied researchers.[1] In recent years, for example, a new gold rush has been triggered by the experimental discovery of a metallic phase at low temperature,[2] in contrast with the scaling theory of localization in two dimensions (2D),[3] and, independently, by the scientific and technological progress on quantum dots, which, at semiconductor interfaces, become nothing but tiny, quasi-two-dimensional quantum disks.[4]

In this context, accurate predictions obtained from a simplified model, such as the ideal 2DEG (strictly 2D electrons interacting via a $1/r$ potential within a uniform, rigid neutralizing background), represent a valuable reference. For example, a recent analytic representation of quantum Monte Carlo correlation energies[5] as a function of spin polarization $\zeta$ and coupling parameter $r_s = 1/\sqrt{\pi n} a_B$ (where $n$ is the density and $a_B$ is the Bohr radius) has been immediately picked by several authors, either because of its relevance to the phase diagram of the 2DEG,[6] or because of the corresponding prediction for the spin suceptibility,[7,8] or, last but not least, because the analytic representation of the correlation energy versus $n$ and $\zeta$ is a key ingredient for the density functional theory of quantum dots.[4,9,10]

Such an interest encouraged us to extend our previous work on energies to the spin-resolved pair-distribution functions $g_{\sigma\sigma'}(\mathbf{r}, \mathbf{r}')$ of the 2DEG, whose accuracy and availability in analytic form may serve a variety of purposes: the exchange-correlation hole and its dependence on the electron density and spin polarization may be relevant to the physics of the metal-insulator bifurcation in 2D[11] and to self-energy theories of the 2DEG,[12] but is also needed for the estimate of the effects of the finite thickness on the spin susceptibility[13] and for the construction of generalized-gradient approximations (GGA) or weighted-density approximations (WDA) of density functionals, in analogy to the 3D case.[14,15] The availability of density functionals better than local-spin-density (LSD) approximations for the 2DEG would, in turn, allow an almost exact description of quantum dots, since the spatial variation of their carrier density is rather weak.[4,10]

In this paper, we exploit the known exact properties of the pair-distribution functions (recalled in Sec. II), and, based on a new set of extensive fixed-node quantum Monte Carlo simulations (described in Sec. III), we propose, in Sec. IV, our analytic representation of (A) the spin-summed pair-distribution function of the ideal two-dimensional interacting electron gas for a wide range of electron densities and spin polarization, and (B) the spin-resolved pair-distribution function of the unpolarized gas. In Sec. V we discuss the quality of such an interpolation, and finally, in Sec. VI , we evaluate the spin-resolved potential energy, of interest in the construction of dynamical exchange-correlation potentials in the spin channel,[16,17] and propose the corresponding analytic representation.

As a result, quantities which are relevant to the physics of semiconductor heterostructures and quantum dots, and/or represent a key ingredient for the construction of two-dimensional spin density functionals beyond the local approximation, are now available, for the first time, in analytic form.

Fortran subroutines for the evaluation of the parametrized quantities are available upon request to gp.giorgi@caspur.it or Giovanni.Bachelet@roma1.infn.it.

## II. DEFINITIONS AND EXACT PROPERTIES

For an electronic system, the pair-distribution functions $g_{\sigma\sigma'}(\mathbf{r}, \mathbf{r}')$, if $n_\sigma(\mathbf{r})$ is the density of electrons with

*present address: Laboratoire de Chimie Théorique, Université Pierre et Marie Curie, Paris, France

spin $\sigma =\uparrow$ or $\downarrow$, are defined as

$$g_{\sigma\sigma'}(\mathbf{r},\mathbf{r}') = \frac{\langle\Phi|\psi^\dagger_\sigma(\mathbf{r})\psi^\dagger_{\sigma'}(\mathbf{r}')\psi_{\sigma'}(\mathbf{r}')\psi_\sigma(\mathbf{r})|\Phi\rangle}{n_\sigma(\mathbf{r})n_{\sigma'}(\mathbf{r}')}, \quad (1)$$

where $\psi^\dagger_\sigma$ and $\psi_\sigma$ are the creation and annihilation field operators, respectively, and $\Phi$ is the ground-state wavefunction. The functions $g_{\sigma\sigma'}$ are thus related to the probability of finding two electrons of prescribed spin orientations at positions $\mathbf{r}$ and $\mathbf{r}'$. The normalization is such that the case of completely independent particles (without exchange and correlation) corresponds to the condition $g_{\sigma\sigma'} = 1$. Hartree atomic units are used throughout this work.

For a two-dimensional uniform electron gas, the functions $g_{\sigma\sigma'}$ only depend on $r = |\mathbf{r} - \mathbf{r}'|$, and parametrically on the density parameter $r_s = 1/\sqrt{\pi\, n}$ and on the spin-polarization parameter $\zeta = (n_\uparrow - n_\downarrow)/n$. The total (spin-summed) pair-distribution function is defined as

$$g = \left(\tfrac{1+\zeta}{2}\right)^2 g_{\uparrow\uparrow} + \left(\tfrac{1-\zeta}{2}\right)^2 g_{\downarrow\downarrow} + \tfrac{1-\zeta^2}{2}\, g_{\uparrow\downarrow}. \quad (2)$$

For small $r$, when two electrons get closer and closer, the behavior of $g_{\sigma\sigma'}$ is governed by the cusp conditions,[18]

$$\left.\frac{\partial}{\partial r} g_{\uparrow\downarrow}(r, r_s, \zeta)\right|_{r=0} = 2\, g_{\uparrow\downarrow}(r=0, r_s, \zeta) \quad (3)$$

$$\left.\frac{\partial}{\partial r} g_{\sigma\sigma}(r, r_s, \zeta)\right|_{r=0} = g_{\sigma\sigma}(r=0, r_s, \zeta) = 0 \quad (4)$$

$$\left.\frac{\partial^3}{\partial r^3} g_{\sigma\sigma}(r, r_s, \zeta)\right|_{r=0} = 2\left.\frac{\partial^2}{\partial r^2} g_{\sigma\sigma}(r, r_s, \zeta)\right|_{r=0}. \quad (5)$$

Eqs. (3) and (5) are due to the dominance of the potential term $1/|\mathbf{r} - \mathbf{r}'|$ in the many-body hamiltonian as $\mathbf{r} \to \mathbf{r}'$; Eq. (4) comes from the Pauli principle.

At this point, it is convenient to introduce the scaled variable $x = k_\mathrm{F} r$, where $k_\mathrm{F} = \sqrt{2}/r_s$ is the Fermi wavevector of the unpolarized gas.

The Fourier transforms of $g_{\sigma\sigma'} - 1$ are the spin-resolved static structure factors,[19] which, for a 2D uniform gas, are

$$S_{\sigma\sigma'}(q, r_s, \zeta) = \delta_{\sigma\sigma'} + \frac{\sqrt{n_\sigma n_{\sigma'}}}{n} \int_0^\infty dx\, [g_{\sigma\sigma'} - 1]\, x\, J_0(qx), \quad (6)$$

where $q = k/k_\mathrm{F}$ is a scaled variable in reciprocal space, and $J_0$ is the Bessel function of order 0. The total (spin-summed) static structure factor is

$$S = \tfrac{1+\zeta}{2}\, S_{\uparrow\uparrow} + \tfrac{1-\zeta}{2}\, S_{\downarrow\downarrow} + \sqrt{1-\zeta^2}\, S_{\uparrow\downarrow}; \quad (7)$$

its long-wavelength (i.e., small-$q$) behavior is determined by the plasma collective mode,[19]

$$S(q \to 0, r_s, \zeta) = \frac{q^{3/2}}{2^{3/4} r_s^{1/2}} + O(q^2), \quad (8)$$

and thus does not depend on $\zeta$.

Usually $g_{\sigma\sigma'}$ (and consequently $S_{\sigma\sigma'}$) is conventionally divided into the (known) exchange and the (unknown) correlation terms,

$$g_{\sigma\sigma'} = g^x_{\sigma\sigma'} + g^c_{\sigma\sigma'}, \quad (9)$$

$$g^x_{\uparrow\downarrow} = 1, \quad (10)$$

$$g^x_{\sigma\sigma} = 1 - \left[\frac{2\, J_1(k^\sigma_\mathrm{F} r)}{k^\sigma_\mathrm{F} r}\right]^2, \quad (11)$$

$$S_{\sigma\sigma'} = S^x_{\sigma\sigma'} + S^c_{\sigma\sigma'}, \quad (12)$$

$$S^x_{\uparrow\downarrow} = 0, \quad (13)$$

$$S^x_{\sigma\sigma} = \frac{2}{\pi}\left[\arcsin\left(\frac{k}{2k^\sigma_\mathrm{F}}\right) + \frac{k}{2k^\sigma_\mathrm{F}}\sqrt{1 - \left(\frac{k}{2k^\sigma_\mathrm{F}}\right)^2}\right] \times \theta(2k^\sigma_\mathrm{F} - k) + \theta(k - 2k^\sigma_\mathrm{F}), \quad (14)$$

where $J_1$ is the first-order Bessel function, $\theta$ is the Heaviside step function, and $k^\uparrow_\mathrm{F} = k_\mathrm{F}\sqrt{1+\zeta}$, $k^\downarrow_\mathrm{F} = k_\mathrm{F}\sqrt{1-\zeta}$. The functions $g^x$ and $S^x$ correspond to a uniform 2-dimensional system of noninteracting fermions; once the scaled variables $x$ and $q$ are used, they do not depend explicitly on $r_s$: $g^x = g^x(x, \zeta)$, $S^x = S^x(q, \zeta)$. In what follows, we use the name *pair-distribution* function for the whole thing ($g = g^x + g^c$, exchange plus correlation), and *pair-correlation* function for its correlation-only contribution $g^c$.

Combining Eqs. (8) and (14), we find the small-$q$ behavior of the spin-summed correlation static structure factor,

$$S^c(q \to 0, r_s, \zeta) = -\frac{2}{\pi}\phi(\zeta)\, q + \frac{q^{3/2}}{2^{3/4} r_s^{1/2}} + O(q^2), \quad (15)$$

where

$$\phi(\zeta) = \frac{\sqrt{1+\zeta} + \sqrt{1-\zeta}}{2} \quad (16)$$

plays the same role of the three-dimensional function $\phi$ of Refs. 20 and 21. As well known from the properties of Fourier transforms, the small-$q$ behavior of $S$ determines the oscillation-averaged long-range part of $g$. We thus see that, individually taken, $g^c$ and $g^x - 1$ have long-range tails $\propto r^{-3}$; but these tails exactly cancel in the pair-distribution function (exchange plus correlation), so that $g - 1 = g^x + g^c - 1$ approches zero as $r^{-7/2}$.

While the long-wavelength limit of the total $S$, Eq. (8), is well known, little is known about the small-$q$ behavior of the spin-resolved $S_{\sigma\sigma'}$ (and hence about the long-range part of $g_{\sigma\sigma'}$). The conservation of the number of particles implies

$$S_{\sigma\sigma'}(q = 0, r_s, \zeta) = 0. \quad (17)$$

In Section IV B we discuss an approximate expression for $S_{\sigma\sigma'}(q \to 0, r_s, \zeta = 0)$ consistent with our QMC results.

Finally, the spin-summed $g^c$ yields the correlation part of the expectation value of the Coulomb potential energy,

$v_c(r_s,\zeta)$, which can be obtained from the correlation energy $\epsilon_c(r_s,\zeta)$ via the virial theorem,[22]

$$\frac{k_{\rm F}}{2}\int_0^\infty dx\, g^c(x,r_s,\zeta) = v_c(r_s,\zeta) = \frac{1}{r_s}\frac{\partial}{\partial r_s}\left[r_s^2\epsilon_c(r_s,\zeta)\right]. \quad (18)$$

## III. QUANTUM MONTE CARLO CALCULATION

The ground-state expectation value $\bar{\mathcal{O}}$ of a local operator $\hat{\mathcal{O}}$, such as the pair-distribution function or the static structure factor, is estimated as

$$\bar{\mathcal{O}} = \langle\Psi(\beta)|\hat{\mathcal{O}}|\Psi(\beta)\rangle/\langle\Psi(\beta)|\Psi(\beta)\rangle \quad (19)$$

using a reptation quantum Monte Carlo (RQMC) algorithm.[23] Here $\Psi$ is a trial function, and $\Psi(\beta) = {\rm e}^{-\beta H/2}\Psi$ can be made sufficiently close to the exact ground state $\Phi$ by choosing the "imaginary time" $\beta$ large enough.

The estimate of Eq. (19) is called "pure", as opposed to the "mixed" estimate $\bar{\mathcal{O}}_{mix} = \langle\Phi|\hat{\mathcal{O}}|\Psi\rangle/\langle\Phi|\Psi\rangle$ usually adopted in connection with the diffusion Monte Carlo (DMC) method.[24] More precisely, previous DMC results for the pair-distribution function of the 2D electron gas[25,26,27] have been based on extrapolated estimates, $\bar{\mathcal{O}}_{ext} = 2\bar{\mathcal{O}}_{mix} - \langle\Psi|\hat{\mathcal{O}}|\Psi\rangle/\langle\Psi|\Psi\rangle$. The bias in $\bar{\mathcal{O}}_{ext}$ is quadratic in the error of the trial function. Such an estimate is often very accurate, but a well converged pure estimate, as obtained in the present work, has the advantage of being independent of the quality of the trial function $\Psi$ (except for its nodal structure, see below).

The RQMC method features a discretized path integral representation of the importance-sampled imaginary time propagator,

$$\begin{aligned}\tilde{G}(R_0 \;\to\; R_P;\beta) &= \Psi(R_P)\langle R_P|{\rm e}^{-\beta H}|R_0\rangle/\Psi(R_0) \quad (20)\\ &= \int dR_1\cdots dR_{P-1}\Pi_{i=0}^{P-1}\tilde{G}(R_i\to R_{i+1};\epsilon),\end{aligned}$$

where $\epsilon=\beta/P$ is the time step and $R_i$ is the set of the $2N$ coordinates of the $N$ electrons at the $i$-th step. We use the standard short-time approximation[24]

$$\begin{aligned}\tilde{G}(R\to R';\epsilon) \;&\simeq\; A{\rm e}^{-[R'-R-\epsilon\nabla\ln\Psi(R)]^2/2\epsilon} \quad (21)\\ &\times\; {\rm e}^{-\epsilon[E_L(R')+E_L(R)]/2},\end{aligned}$$

where $E_L(R) = H\Psi(R)/\Psi(R)$ is the "local energy", and $A=(2\pi\epsilon)^{-N}$ is a normalization constant. Replacement of Eqs. (21) and (22) into (19) yields an integral amenable to Monte Carlo evaluation, using a generalized Metropolis algorithm to sample paths in an enlarged configuration space, $X=\{R_0,\cdots,R_P\}$.

In our simulations we consider $N_\uparrow$ spin-up and $N_\downarrow$ spin-down particles in a square box with periodic boundary conditions. The spin-resolved pair-distribution functions are obtained[28] averaging $VdN_{\sigma\sigma'}(r')/[N_\sigma(N_{\sigma'}-\delta_{\sigma\sigma'})2\pi r\Delta]$ in the middle slice of the path during the simulation, where $V$ is the volume of the simulation cell, $dN_{\sigma\sigma'}(r')$ is the number of electron pairs with distance $r'$ between $r-\Delta/2$ and $r+\Delta/2$. The structure factors are computed analogously, for vectors $\mathbf{k}$ in the reciprocal lattice of the simulation cell, by averaging $\rho_\sigma(\mathbf{k})\rho_{\sigma'}(-\mathbf{k})/(N_\sigma N_{\sigma'})^{1/2}$, where $\rho_\sigma(\mathbf{k}) = \sum_j \exp(-i\mathbf{k}\cdot\mathbf{r}_j)$ is the density fluctuation of electrons with spin $\sigma$. The total number of particles is 42, 50, 50 and 45 for polarization 0, 0.48, 0.80 and 1, respectively. By repeating simulations for different system sizes in the unpolarized case, finite size effects on the pair-distribution function have been estimated to be of order 0.01. The systematic bias due to finite projection time and finite time step can be kept within this level by suitable choices of the parameters $\beta$ and $\epsilon$. In our simulations, this results in paths of 501 time slices.

We avoid the fermion sign problem using the fixed node approximation (FNA),[24] whereby the paths are not allowed to cross the nodes of the trial function. The FNA, which gives the lowest energy upper bound consistent with the nodal structure of the trial function, is the only source of uncontrolled approximation in the present calculation. In order to gauge the sensitivity of the computed pair-distribution function on the nodal structure of $\Psi$, we have performed our simulations using two trial functions with different nodes.

Our first trial function is of the simplest Jastrow-Slater form $\Psi(R)=J(R)S(R)$. Here $J(R)=\Pi_{i<j}\exp(-u(r_{ij}))$, $r_{ij}$ being the distance between the electrons $i$ and $j$, is a symmetric Jastrow factor; it describes pair correlations through the function $u(r)$, which is optimized (by minimizing the variational energy) for each density and polarization; it's always positive, so it does not alter the nodal structure, which is entirely determined by the other factor $S(R)$, a product of two Slater determinants (one for each spin component) of plane-wave one-particle orbitals $\exp(\mathbf{k}_i\cdot\mathbf{r}_j)$.

Our second trial function has the same Jastrow factor, but its nodal structure is more accurate, since it includes "backflow" correlations[27,29] by replacing the electron coordinates $\mathbf{r}_j$ in the Slater determinants with "quasi-coordinates"

$$\mathbf{x}_j = \mathbf{r}_j + \sum_{i\neq j}\eta(r_{ij})(\mathbf{r}_i-\mathbf{r}_j), \quad (22)$$

where $\eta(r)$ is another function to be optimized for each density and polarization.

In a previous variational calculation[27] the difference between the pair-distribution function calculated with the simple Slater-Jastrow and the backflow trial function was found to be of order 0.03. Here we find that, in a fixed-node calculation, such effect is even smaller: Figure 1 shows the difference in $g_{\uparrow\uparrow}$ and $g_{\uparrow\downarrow}$, computed with either plane-wave or backflow nodes, for $r_s=2$ and 20 at zero polarization. In the worst case (large $r_s$, lower panel) these differences are half as large as found in the variational case,[27] while for small $r_s$ (upper panel) they

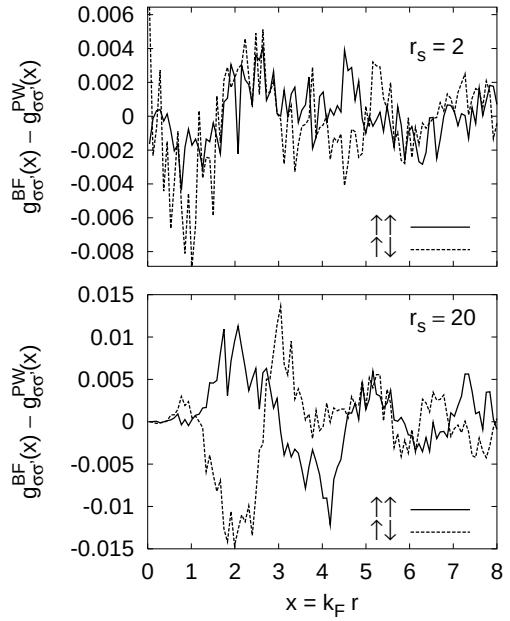



FIG. 1: Numerical difference between the spin-resolved pair-distribution functions $g^{BF}_{\sigma\sigma'} - g^{PW}_{\sigma\sigma'}$ at $r_s = 2$ (upper panel) and $r_s = 20$ (lower panel), as obtained from two fixed-node simulations with different nodal structures. The superscript indicates backflow ($BF$) or plane-wave ($PW$) nodes.

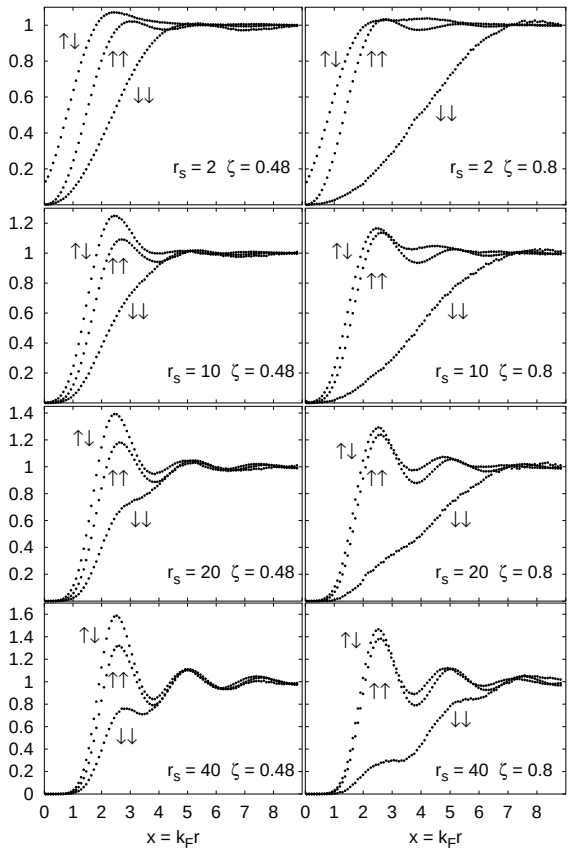



FIG. 2: Sample of spin-resolved pair-distribution functions as directly obtained from our QMC simulations (no fitting here).

are much smaller than that. These differences are essentially invisible on the scale of our $g_{\sigma\sigma'}(r, r_s, \zeta)$ calculated with plane-wave nodes, some samples of which are shown Figure 2. As a consequence, an analytic representation of the spin-summed $g(r, r_s, \zeta)$ and of $g_{\sigma\sigma'}(r, r_s, \zeta = 0)$ (see next Sec. IV) based on the plane-wave results, as the one presented here, happens to give an equally good representation of the backflow results, because the difference due to the improved nodal structure is either comparable or smaller than the fitting error.

## IV. ANALYTIC REPRESENTATION

In this section we describe our analytic representations of the spin-summed pair-correlation function $g^c(x, r_s, \zeta)$ valid for $1 \le r_s \le 40$ and $0 \le \zeta \le 1$, and of the spin-resolved $g^c_{\sigma\sigma'}(x, r_s, \zeta)$ for $\zeta = 0$ and $1 \le r_s \le 10$. These functions are built along the lines of Refs. 20,21 and of Ref. 31 for the 3D case.

The strategy is the following. We build the spin-summed $g^c$ as a sum of three terms: long-range, short-range, and oscillatory. The long-range term is taken from the random-phase approximation (RPA) and multiplied by a cutoff function which quenches its short-range contribution. The short-range part is built according to the cusp conditions of Eqs. (3)-(5), as a weighted sum of $\uparrow\uparrow$, $\uparrow\downarrow$ and $\downarrow\downarrow$ terms which, in turn, have been determined for $\zeta = 0$ by a fitting procedure to the QMC results. For $\zeta \neq 0$, an exchange-like $\zeta$-dependence of these $\sigma\sigma'$ short-range coefficients has been assumed. The oscillatory part is empirical, being entirely determined by a fit to the QMC data. The analytic function $g^c$ is also constrained, via Eq. (18), to reproduce our parametrized correlation energy of Ref. 5.

The analytic parametrization of the spin-resolved $g^c_{\sigma\sigma'}$ is more difficult, because less is known about its exact properties. We had to rely more heavily on our QMC data, and, for the time being, we successfully interpolated $g^c_{\uparrow\downarrow}$ only in the unpolarized case ($\zeta = 0$) and for $r_s \in [1, 10]$. This parametrization, combined with the one for the total $g^c$ also yields $g^c_{\uparrow\uparrow} = g^c_{\downarrow\downarrow} = 2g^c - g^c_{\uparrow\downarrow}$. We build $g^c_{\uparrow\downarrow}$ using a functional form similar to the one just described for the total $g^c$: a sum of a long-range term, a short-range term, and an oscillatory term. The long-range term is obtained by a modification, consistent with our QMC data, of the long-range analytic form appropriate for the total (spin-summed) $g^c$. The short-range term is simply the $\uparrow\downarrow$ part of the total $g^c$. The oscillatory part

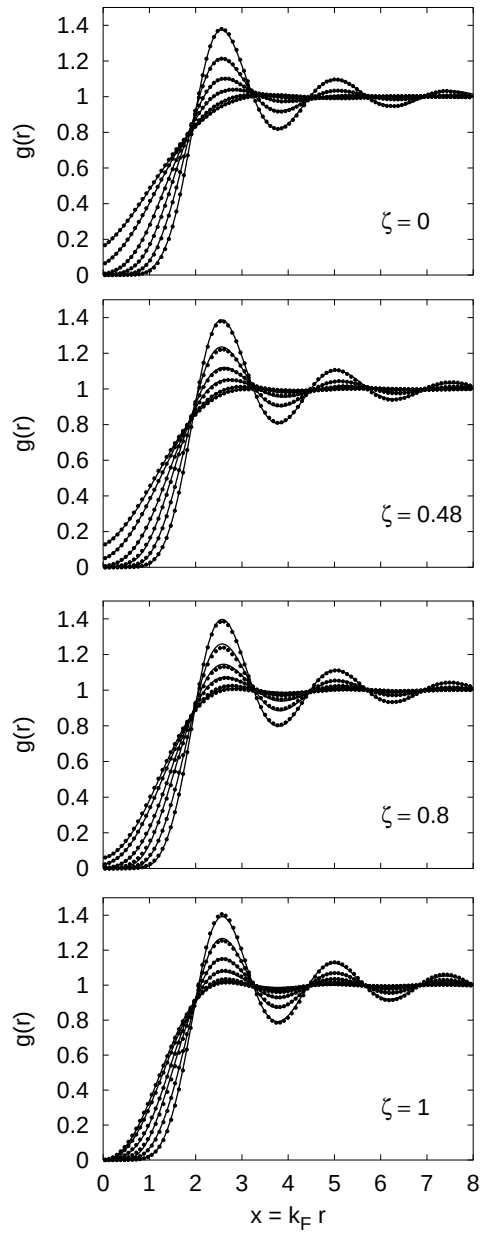



FIG. 3: Spin-summed pair-distribution function (exchange plus correlation: $g = g^x + g^c$, see text) for four different values of the spin-polarization parameter $\zeta$, and for $r_s = 1$, 2, 5, 10, 20, and 40 (larger $r_s$ values have stronger oscillations). The dots correspond to our QMC data, the solid lines to our analytic representation. Error bars are comparable with the dot size.

is, again, empirical. Because the short-range parts of the total $g^c$ and of $g^c_{\uparrow\downarrow}$ share some parameters, we performed a simultaneous, global, three-dimensional $(x, r_s, \zeta)$ fit of $g^c(x, r_s, \zeta)$ and $g^c_{\uparrow\downarrow}(x, r_s, \zeta = 0)$. This procedure and all the relevant equations are detailed in the next subsections.

### A. Spin-summed pair-correlation function

We parametrize the spin-summed $g^c$ as

$$g^c = [g_{\rm LR}(x) + g_{\rm oscill}(x)]\, F_{\rm cut}(x) + e^{-d\,x^2} \sum_{n=0}^{6} c_n x^n, \quad (23)$$

where $g_{\rm LR}$ is a long-ranged function whose Fourier transform exactly recovers Eq. (15), $g_{\rm oscill}$ is an oscillating function to be fitted to the QMC data, and the last term in the r.h.s takes care of the short-range properties. The function $F_{\rm cut}(x)$ quenches[21] the short-range contribution of $(g_{\rm LR} + g_{\rm oscill})$,

$$F_{\rm cut} = 1 - e^{-d\,x^2} \left(1 + d\,x^2 + \tfrac{1}{2} d^2 x^4 + \tfrac{1}{6} d^3 x^6\right) . \quad (24)$$

The parameter $d(r_s)$ determines the mixing of long-range and short-range terms in Eq. (23).

#### 1. Long-Range part

The long-range part is built with the same procedure used for the 3D case in Refs. 20,21 and 38, and detailed in Appendix A,

$$g_{\rm LR}(x, r_s, \zeta) = 2\,\phi^5(\zeta)\, r_s^2\, \frac{f_1(v)}{x}, \quad (25)$$

where $v = \sqrt{2} r_s \phi^2 x$ is another scaled variable, and $\phi(\zeta)$ is given by Eq. (16). The function $f_1(v)$ is reported in Appendix A.

#### 2. Short-Range part

The short-range part of our $g^c$ is the last term in the r.h.s of Eq. (23). We have

$$c_0 = \tfrac{1-\zeta^2}{2}\, g^c_{\uparrow\downarrow}(0) \quad (26)$$

$$c_1 = \tfrac{2}{k_{\rm F}}\, \tfrac{1-\zeta^2}{2}\, [g^c_{\uparrow\downarrow}(0) + 1] \quad (27)$$

$$c_2 = d\,c_0 + \tfrac{1-\zeta^2}{2}\, a_2^{\uparrow\downarrow} + \left(\tfrac{1+\zeta}{2}\right)^2 a_2^{\uparrow\uparrow} + \left(\tfrac{1-\zeta}{2}\right)^2 a_2^{\downarrow\downarrow} - \tfrac{1}{8}(1 + 3\,\zeta^2) \quad (28)$$

$$c_3 = d\,c_1 + \tfrac{1-\zeta^2}{2}\, a_3^{\uparrow\downarrow} + \left(\tfrac{1+\zeta}{2}\right)^2 a_3^{\uparrow\uparrow} + \left(\tfrac{1-\zeta}{2}\right)^2 a_3^{\downarrow\downarrow} \quad (29)$$

where $a_n^{\sigma\sigma'}$ are the short-range coefficients of the spin-resolved pair-distribution functions,

$$g_{\sigma\sigma'}(x \to 0, r_s, \zeta) = \sum_n a_n^{\sigma\sigma'} x^n, \quad (30)$$

and

$$a_3^{\sigma\sigma} = \frac{2}{3 k_{\rm F}} a_2^{\sigma\sigma}. \quad (31)$$

The pair-correlation function at zero electron-electron distance, or "on-top" value $g^c_{\uparrow\downarrow}(0) \equiv a_0^{\uparrow\downarrow} - 1$, has been parametrized as

$$g^c_{\uparrow\downarrow}(0) = [1 + (a - 1.372)\, r_s + b\, r_s^2 + c\, r_s^3]\, e^{-a\, r_s} - 1. \quad (32)$$

The parameters $a = 1.46$, $b = 0.258$, $c = 0.00037$ are fitted to the QMC results; the exact high-density slope, 1.372, is taken from Ref. 39.

As said at the beginning of this section, we determine the spin-resolved short-range coefficients for the $\zeta = 0$ case, and then we assume an exchange-like $\zeta$-dependence. This means that in Eqs. (26)-(29) the values of $g^c_{\uparrow\downarrow}(0)$, $a_2^{\uparrow\downarrow}$ and $a_3^{\uparrow\downarrow}$ only depend on $r_s$ (not on $\zeta$), and that the coefficients $a_2^{\uparrow\uparrow}$ and $a_2^{\downarrow\downarrow}$ have the simple $\zeta$ dependence

$$a_2^{\uparrow\uparrow}(r_s, \zeta) = \tfrac{1}{4}(1 + \zeta) a_p(r_s), \quad (33)$$

with $a_2^{\downarrow\downarrow}(r_s, \zeta) = a_2^{\uparrow\uparrow}(r_s, -\zeta)$.

The linear parameters $c_4$ and $c_5$ will be used to constrain $g^c$ to yield the correlation energy of Ref. 5 and to fulfill the particle-conservation sum rule [$S(q = 0, r_s, \zeta) = 0$], as in Ref. 21. The parameter $c_6(r_s, \zeta)$ is used to give more variational freedom to our $g^c$ for an accurate fit of the QMC data at higher $r_s$.

### 3. Oscillatory part

The oscillatory part of our $g^c$ is similar to the form used by Tanatar and Ceperley,[25]

$$g_{\rm oscill} = \frac{m_1}{x + 1}\, e^{-m_2\, x} \cos(m_3\, x + m_4) \quad (34)$$

which is able to accurately fit the QMC data at low densities. The exponential cutoff ensures that $g_{\rm oscill}$ does not alter the long-range properties embedded in $g_{\rm LR}$. The parameters $m_i$ depend on both $r_s$ and $\zeta$.

### 4. Sum rules

As said, the role of the parameters $c_4$ and $c_5$ which appear in the short-range part of our $g_c$ is to fulfill the normalization sum rule [$S^c(q = 0) = 0$] and to recover the correlation energy $\epsilon_c(r_s, \zeta)$ of Ref. 5. We obtain

$$c_4 = 8\, d^2 \frac{15\sqrt{d}\sqrt{\pi}\, C_e - 16\, d\, C_s}{45\pi - 128} \quad (35)$$

$$c_5 = 16\, d^3 \frac{3\sqrt{d}\sqrt{\pi}\, C_s - 8\, C_e}{45\pi - 128}, \quad (36)$$

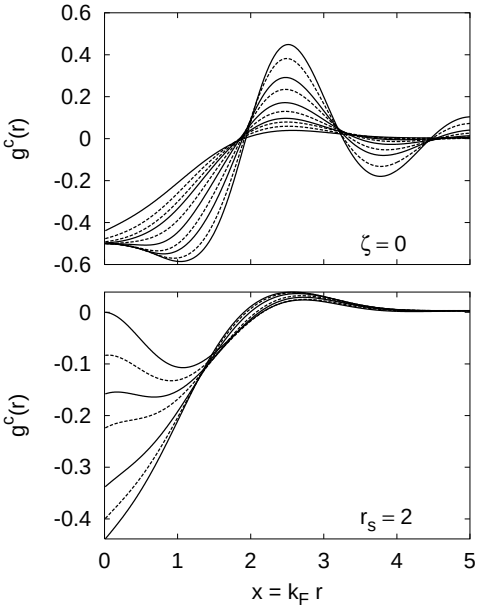



FIG. 4: Spin-summed pair-correlation functions $g^c$ from our analytic representation. Upper panel: for $\zeta = 0$, we show $g^c$ for $r_s = 2, 3, 4, 5, 7, 10, 15, 20, 30, 40$; stronger oscillations correspond to higher $r_s$ values. The solid lines correspond to $r_s = 2, 5, 10, 20, 40$, for which our $g^c$ accurately fits the QMC data; the dashed lines are the results for intermediate values of $r_s$. Lower panel: for $r_s = 2$, we show $g^c$ for different values of the spin-polarization $\zeta = 0, 0.3, 0.48, 0.7, 0.8, 0.9, 1$; more negative "on-top" values $g^c(x = 0)$ correspond to lower values of $\zeta$. The solid lines correspond to $\zeta = 0, 0.48, 0.8, 1$, for which our $g^c$ accurately fits the QMC data. The dashed lines correspond to intermediate values of $\zeta$.

with

$$C_s = -\frac{c_0}{2d} - \frac{c_1\sqrt{\pi}}{4d^{3/2}} - \frac{c_2}{2d^2} - c_3\frac{3\sqrt{\pi}}{8d^{5/2}} - \frac{3\, c_6}{d^4} + 2\phi^5 r_s^2\, s_{\rm LR} - s_{\rm oscill} \quad (37)$$

$$C_e = -\frac{c_0\sqrt{\pi}}{2\sqrt{d}} - \frac{c_1}{2d} - \frac{c_2\sqrt{\pi}}{4d^{3/2}} - \frac{c_3}{2d^2} - c_6\frac{15}{16}\frac{\sqrt{\pi}}{d^{7/2}} - 2\phi^5 r_s^2 E_{\rm LR} - E_{\rm oscill} + \sqrt{2} r_s\, v_c \quad (38)$$

$$s_{\rm LR} = \int_0^\infty f_1(v)\, [1 - F_{\rm cut}(x)]\, dx \quad (39)$$

$$E_{\rm LR} = \int_0^\infty \frac{f_1(v)}{x} F_{\rm cut}(x)\, dx \quad (40)$$

$$s_{\rm oscill} = \int_0^\infty g_{\rm oscill}(x)\, x\, F_{\rm cut}(x)\, dx \quad (41)$$

$$E_{\rm oscill} = \int_0^\infty g_{\rm oscill}(x) F_{\rm cut}(x)\, dx, \quad (42)$$

and $v_c(r_s, \zeta)$ given in Eq. (18). Equations (39)-(42) are evaluated numerically for given $r_s$ and $\zeta$.

| total $g^c$: | | | |
|---|---|---|---|
| $\delta_1 = 0.293$ | $\delta_2 = 0.136$ | | |
| $\gamma_1^{(2)} = 0.0586$ | $\gamma_2^{(2)} = 0.153$ | $\gamma_3^{(2)} = 0.476$ | |
| $\gamma_1^{(3)} = 0.0457$ | $\gamma_2^{(3)} = 0.0427$ | $\gamma_3^{(3)} = 0.229$ | |
| $\lambda_1 = 0.0377$ | $\lambda_2 = 0.123$ | $\lambda_3 = 0.68$ | |
| $\beta_1 = 0.828$ | $\eta_1 = 0.11$ | $\beta_2 = 445$ | $\eta_2 = -82$ |
| $p_1^{(1)} = 3.69$ | $q_1^{(1)} = -0.987$ | $p_2^{(1)} = 4.74$ | $q_2^{(1)} = 2.83$ |
| $p_1^{(2)} = 0.92$ | $q_1^{(2)} = -0.443$ | $p_2^{(2)} = 0.044$ | $q_2^{(2)} = -0.0151$ |
| $p_1^{(3)} = 2.14$ | $q_1^{(3)} = 0.394$ | $p_2^{(3)} = 0.045$ | $q_2^{(3)} = -0.0299$ |
| $p_1^{(4)} = 6.39$ | $q_1^{(4)} = -0.592$ | $p_2^{(4)} = 2.7 \cdot 10^{-4}$ | $q_2^{(4)} = -1.8 \cdot 10^{-4}$ |
| $g^c_{\uparrow\downarrow}$: | | | |
| $\gamma_1^{(5)} = 1.1$ | $\gamma_2^{(5)} = 29$ | | |
| $\nu_1^{(1)} = 0.479$ | $\nu_2^{(1)} = 0.029$ | | |
| $\nu_1^{(2)} = 0.6$ | | | |
| $\nu_1^{(3)} = 1.99$ | $\nu_2^{(3)} = 0.0014$ | | |
| $\nu_1^{(4)} = 1.437$ | $\nu_2^{(4)} = 0.1$ | | |

TABLE I: Optimal parameters for the analytic representation of $g^c(x, r_s, \zeta)$ and $g^c_{\uparrow\downarrow}(x, r_s, \zeta = 0)$ as described in Sec. IV.

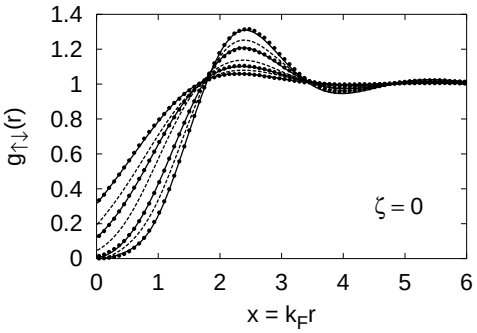



FIG. 5: $\uparrow\downarrow$ pair-distribution function (exchange plus correlation, see text) for $\zeta = 0$ and $r_s = 1$, 1.5, 2, 3, 5, 7, 10 (the larger $r_s$ values have stronger oscillations). The dots correspond to our QMC data for $r_s = 1$, 2, 5, 10; the solid lines is our analytic representation at the same $r_s$-values. Dashed lines correspond to our analytic representation for the other values of $r_s$.

#### 5. *Fitting parameters*

The parameters $d(r_s)$, $a_2^{\uparrow\downarrow}(r_s)$, $a_3^{\uparrow\downarrow}(r_s)$, $a_p(r_s)$, $c_6(r_s, \zeta)$, $m_i(r_s, \zeta)$ are used to fit the QMC data. Their $r_s$ and $\zeta$ dependence is smooth and allows for an analytic representation of $g^c(x, r_s, \zeta)$ valid at all $r_s \in [1, 40]$ and $\zeta \in [0, 1]$:

$$d(r_s) = \frac{\delta_1 + \delta_2 r_s^2}{1 + \delta_2 r_s^2} \quad (43)$$

$$a_2^{\uparrow\downarrow}(r_s) = (-\gamma_1^{(2)} r_s + \gamma_2^{(2)} r_s^2)\, e^{-\gamma_3^{(2)} r_s} \quad (44)$$

$$a_3^{\uparrow\downarrow}(r_s) = (-\gamma_1^{(3)} r_s + \gamma_2^{(3)} r_s^2)\, e^{-\gamma_3^{(3)} r_s} \quad (45)$$

$$a_p(r_s) = (1 - \lambda_1 r_s + \lambda_2 r_s^2)\, e^{-\lambda_3 r_s} \quad (46)$$

$$c_6(r_s, \zeta) = \gamma_1^{(6)}(\zeta) e^{-\gamma_2^{(6)}(\zeta)/r_s^2} \quad (47)$$

$$m_1(r_s, \zeta) = \mu_1^{(1)}(\zeta) e^{-\mu_2^{(1)}(\zeta)/r_s} \quad (48)$$

$$m_2(r_s, \zeta) = \frac{\mu_1^{(2)}(\zeta)}{1 + \mu_2^{(2)}(\zeta) r_s} \quad (49)$$

$$m_3(r_s, \zeta) = \frac{\mu_1^{(3)}(\zeta) + 2.7\mu_2^{(3)}(\zeta) r_s}{1 + \mu_2^{(3)}(\zeta) r_s} \quad (50)$$

$$m_4(r_s, \zeta) = \frac{\mu_1^{(4)}(\zeta) + 5.36\mu_2^{(4)}(\zeta) r_s^2}{1 + \mu_2^{(4)}(\zeta) r_s^2}. \quad (51)$$

The functional form of the short-range coefficients $a_n^{\sigma\sigma'}$ is very similar to the one used for the 3D case in Ref. 40; the corresponding parameters are determined by simultaneously fitting the data for $g^c_{\uparrow\downarrow}$ (see next Section) and those for the total $g^c$. The parameter $c_6$ only comes into play at high $r_s$: its functional form, Eq. (47), makes it vanish very rapidly as $r_s$ decreases. The same argument applies to the oscillatory part, whose magnitude is determined by the parameter $m_1$ of Eq. (48). The low-density limit of the parameters $m_3$ and $m_4$, 2.7 and 5.36 in Eqs. (50) and (51), are taken from an oversimplified model of localization on the sites of a triangular lattice.[30] The $\zeta$ dependence of the parameters $\gamma_i^{(6)}$ and $\mu_i^{(n)}$ is well represented by a quadratic form:

$$\gamma_i^{(6)}(\zeta) = \beta_i + \eta_i \zeta^2 \quad (52)$$

$$\mu_i^{(n)}(\zeta) = p_i^{(n)} + q_i^{(n)} \zeta^2. \quad (53)$$

The final 32 free parameters (plus 9 parameters for $g^c_{\uparrow\downarrow}$, detailed in the next section) are fitted to our data set (100 values of $x$ for each $r_s = 1, 2, 5, 10, 20, 40$ and $\zeta = 0, 0.48, 0.8, 1$ plus those for $g^c_{\uparrow\downarrow}$ at $\zeta = 0$ and $r_s = 1, 2, 5, 10$ – a total of 2800 data), and are reported in Table I.

### B. Spin-resolved pair-correlation functions ($\zeta = 0$)

We parametrize the $\uparrow\downarrow$ correlation function with a functional form similar to the one used for the spin-summed $g^c$,

$$g^c_{\uparrow\downarrow} = [g^{\uparrow\downarrow}_{\rm LR}(x) + g^{\uparrow\downarrow}_{\rm oscill}(x)]\, F_{\rm cut}(x) + e^{-d\,x^2} \sum_{n=0}^{5} c_n^{\uparrow\downarrow} x^n, \quad (54)$$

where the function $F_{\rm cut}(x)$ and the parameter $d(r_s)$ are given in Eqs. (24) and (43), respectively.

#### 1. *Long-Range part*

While the long-range part of the spin-summed $g^c$, Eq. (25), can be obtained from RPA, the spin-resolution is more problematic. Nonetheless, RPA can give some hints,[31] especially in the $r_s \to 0$ limit. From RPA we

obtain, up to $O(q^2)$,

$$S^{c\,(\mathrm{RPA})}_{\sigma\sigma'}(q\to 0, r_s, \zeta) = -\frac{q}{\pi}\xi_{\sigma\sigma'}(\zeta) + \frac{q^{3/2}}{2^{3/4} r_s^{1/2}} \frac{\sqrt{n_\sigma n_{\sigma'}}}{n}, \tag{55}$$

with $\xi_{\uparrow\downarrow}(\zeta) = 1$, $\xi_{\uparrow\uparrow}(\zeta) = 2/\sqrt{1+\zeta} - \sqrt{1-\zeta}/\sqrt{1+\zeta}$, and $\xi_{\downarrow\downarrow}(\zeta) = \xi_{\uparrow\uparrow}(-\zeta)$.

Here, we only treat the $\zeta = 0$ case, for which we also produced spin-resolved static structure factors with QMC. We write the small-$q$ part of $S^c_{\sigma\sigma'}$ as the RPA result plus an $r_s$-dependent correction, similar to the 3D case,[32] i.e., up to $O(q^2)$,

$$S^c_{\sigma\sigma'}(q\to 0, r_s, \zeta = 0) = -q\left[\frac{1}{\pi} + \alpha_{\sigma\sigma'}(r_s)\right] + \frac{q^{3/2}}{2^{7/4} r_s^{1/2}}, \tag{56}$$

with $\alpha_{\uparrow\uparrow}(r_s) = -\alpha_{\uparrow\downarrow}(r_s)$. This small-$q$ behavior embodies the following properties: (i) the corresponding spin-resolved pair-distribution function $g_{\sigma\sigma'}(r)$ are more long-ranged[33] than the spin-summed $g(r)$, (ii) parallel- and antiparallel-spin correlations give identical contributions to the plasma collective mode. The correction $\alpha_{\uparrow\downarrow}(r_s)$ has been determined from the QMC results in reciprocal space for $1 \le r_s \le 10$, and is well represented by

$$\alpha_{\uparrow\downarrow}(r_s) = 0.00914\, r_s. \tag{57}$$

Thus, for the spin-resolved long-range part we use a scaling law similar to the one of Eq. (25),

$$g^{\uparrow\downarrow}_{\mathrm{LR}}(x, r_s, \zeta) = 2\,\phi^5(\zeta)\, r_s^2\, \frac{\tilde{f}_1(v, \alpha_{\uparrow\downarrow})}{x}; \tag{58}$$

the function $\tilde{f}_1(v,\alpha)$ is described in Appendix B.

### 2. Short-Range part

The short-range part of $g^c_{\uparrow\downarrow}$ is the $\uparrow\downarrow$ part of the total $g^c$ [see Eqs. (26)-(29)]. We thus have

$$c_0^{\uparrow\downarrow} = g^c_{\uparrow\downarrow}(0) \tag{59}$$

$$c_1^{\uparrow\downarrow} = \frac{4}{k_{\mathrm{F}}}[g^c_{\uparrow\downarrow}(0) + 1] \tag{60}$$

$$c_2^{\uparrow\downarrow} = d\, c_0^{\uparrow\downarrow} + a_2^{\uparrow\downarrow} \tag{61}$$

$$c_3^{\uparrow\downarrow} = d\, c_1^{\uparrow\downarrow} + a_3^{\uparrow\downarrow}, \tag{62}$$

where $g^c_{\uparrow\downarrow}(0)$, $a_2^{\uparrow\downarrow}$, and $a_3^{\uparrow\downarrow}$ are given in Eqs. (32), (44), and (45), respectively.

The linear parameter $c_4^{\uparrow\downarrow}$ is used to fulfill the normalization sum rule of Eq. (17); the parameter $c_5^{\uparrow\downarrow}(r_s)$, instead, increases the variational flexibility of $g^c_{\uparrow\downarrow}$, and is fitted to the QMC data.

### 3. Oscillatory part

For $g^c_{\uparrow\downarrow}$ we use the same form [Eq. 34] of the total $g^c$,

$$g^{\uparrow\downarrow}_{\mathrm{oscill}} = \frac{m_1^{\uparrow\downarrow}}{x+1}\, e^{-m_2^{\uparrow\downarrow} x} \cos(m_3^{\uparrow\downarrow} x + m_4^{\uparrow\downarrow}). \tag{63}$$

The parameters $m_i^{\uparrow\downarrow}$ depend on $r_s$ and are fitted to the QMC data.

### 4. Sum rule

The sum rule Eq. (17) determines the linear parameter $c_4^{\uparrow\downarrow}$,

$$c_4^{\uparrow\downarrow} = d^3\, C_s^{\uparrow\downarrow}, \tag{64}$$

with

$$C_s^{\uparrow\downarrow} = -\frac{c_0^{\uparrow\downarrow}}{2d} - \frac{c_1^{\uparrow\downarrow}\sqrt{\pi}}{4d^{3/2}} - \frac{c_2^{\uparrow\downarrow}}{2d^2} - c_3^{\uparrow\downarrow}\frac{3\sqrt{\pi}}{8d^{5/2}} - c_5^{\uparrow\downarrow}\frac{15\sqrt{\pi}}{16\, d^{7/2}} + 2\phi^5 r_s^2\, s^{\uparrow\downarrow}_{\mathrm{LR}} - s^{\uparrow\downarrow}_{\mathrm{oscill}}, \tag{65}$$

$$s^{\uparrow\downarrow}_{\mathrm{LR}} = \int_0^\infty \tilde{f}_1(v, \alpha_{\uparrow\downarrow})\,[1 - F_{\mathrm{cut}}(x)]\, dx \tag{66}$$

$$s^{\uparrow\downarrow}_{\mathrm{oscill}} = \int_0^\infty g^{\uparrow\downarrow}_{\mathrm{oscill}}(x)\, x\, F_{\mathrm{cut}}(x)\, dx. \tag{67}$$

### 5. Fitting parameters

From the global fit described for the total $g^c$, we also find the $r_s$ dependence of the coefficients $c_5^{\uparrow\downarrow}$ and $m_i^{\uparrow\downarrow}$:

$$c_5^{\uparrow\downarrow}(r_s) = \gamma_1^{(5)} e^{-\gamma_2^{(5)}/r_s^2} \tag{68}$$

$$m_1^{\uparrow\downarrow}(r_s) = \frac{\nu_1^{(1)} r_s}{1 + \nu_2^{(1)} r_s} \tag{69}$$

$$m_2^{\uparrow\downarrow}(r_s) = \nu_1^{(2)} \tag{70}$$

$$m_3^{\uparrow\downarrow}(r_s) = \nu_1^{(3)} + \frac{\nu_2^{(3)} r_s^2}{1 + \nu_2^{(3)} r_s^2} \tag{71}$$

$$m_4^{\uparrow\downarrow}(r_s) = \frac{\nu_1^{(4)}}{1 + \nu_2^{(4)} r_s}. \tag{72}$$

The values of $\gamma_i^{(5)}$ and $\nu_i^{(n)}$ are reported in Table I.

## V. RESULTS

A pictorial evidence of the quality of our analytic representation clearly emerges from Fig. 3, where we show our analytic representation for the spin-summed $g(r)$, together with the corresponding QMC data, for $r_s = 1$, 2,

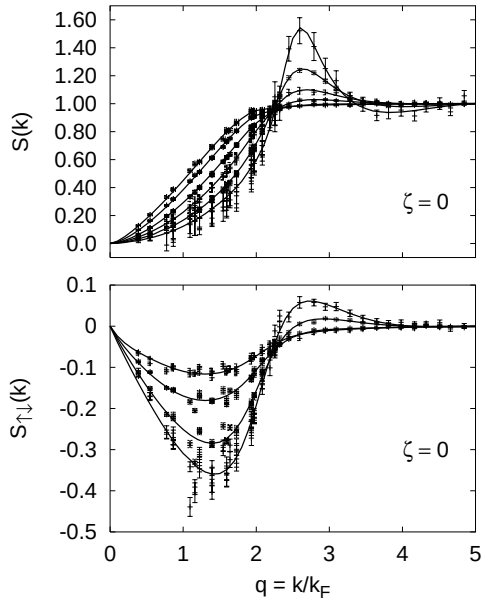



FIG. 6: Upper panel: total (spin-summed) structure factor as directly obtained from our QMC simulations (data with error bars) and as a Fourier transform of our analytic representation of $g^c$ (solid lines), for $r_s = 1, 2, 5, 10, 20, 40$. Higher peaks correspond to larger $r_s$. Lower panel, same comparison for the $\uparrow\downarrow$ static structure factor: the data with error bars are QMC simulations and the solid lines are Fourier transforms of our analytic $g^c_{\uparrow\downarrow}$. Here the $r_s$ values are 1, 2, 5, and 10 and the larger deviations from the noninteracting value $S_{\uparrow\downarrow} = 0$ correspond to larger $r_s$ values.

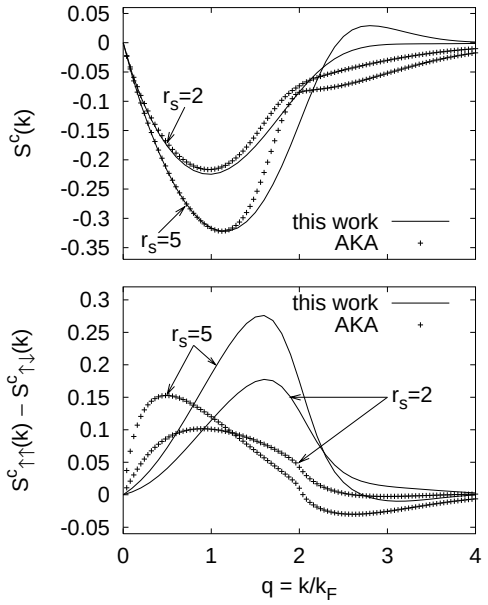



FIG. 7: Upper panel: spin-summed correlation static structure factors from our analytic representation of $g^c$ and from the Atwal, Khalil and Ashcroft[34] (AKA) dynamical local-field factor. Lower panel: the same comparison is done for the spin channel (correlation only, $\uparrow\uparrow - \uparrow\downarrow$). All curves are for $\zeta = 0$.

5, 10, 20 and 40 and four different values of the spin-polarization $\zeta$. Figure 4, instead, shows that our analytic $g^c(r, r_s, \zeta)$ smoothly interpolates the QMC data not only as a function of $x = k_F r$, as e.g. shown in the previous Figure 3, but also as a function of $r_s$ (upper panel) and of $\zeta$ (lower panel). Figure 5 summarizes similar results for $g^c_{\uparrow\downarrow}$ at $\zeta = 0$. The static structure factors for $\zeta = 0$ are reported in Fig. 6. In the upper panel, we compare the total $S(q)$ corresponding to our analytic $g^c$ with our QMC calculation (see Sec. III); the agreement indicates that the long-range part ($q \to 0$ limit of $S$) of the analytic $g^c$ has been accurately described. In the lower panel, we show similar results for $S_{\uparrow\downarrow}(q)$. We see that the long-range ($q \to 0$) spin-resolution of Eq. (56) is consistent with the QMC results.

Recently, Atwal, Khalil and Ashcroft[34] (AKA) have presented a parametrization of the dynamical local-field factors (spin-symmetric, $\uparrow\uparrow + \downarrow\downarrow$, and spin-antisymmetric, $\uparrow\uparrow - \downarrow\downarrow$) for the $\zeta = 0$ 2D electron gas, as a function of the wavevector $q$ and of the imaginary frequency $i\omega$. Following the analysis carried on for the 3D electron gas by Lein, Gross and Perdew,[35] Asgari *et al.*[36] have compared the wavector decomposition of the correlation energy resulting from the AKA spin-symmetric local field factor with the one resulting from our present work, based on QMC results, for $r_s = 1$. In the upper panel of our Fig. 7 we make a similar comparison (in this case at full coupling strength) for $r_s = 2$ and $r_s = 5$. In the lower panel of the same figure we also compare the results from the AKA spin-antysimmetric local-field factors. We see that the spin-summed AKA $S^c(q)$ is in fair agreement with our result for $q \lesssim 1.5$, where both curves recover the exact behavior of Eq. (15). The spin-antisymmetric AKA curves are, instead, quite different from our result, even for small $q$. This discrepancy probably comes from an inaccurate description of the high-$\omega$ behavior of the $q \to 0$ limit of the AKA parametrization for the spin channel.[17] In particular, Eq. (26) of AKA yields a formally divergent result when combined with the known limiting behavior[37] $S_{\uparrow\downarrow}(q \to \infty) \propto q^{-3}$.

## VI. SPIN-RESOLVED POTENTIAL ENERGY

The correlation part of the potential energy, $v_c(r_s, \zeta)$ of Eq. (18), can be divided into $\uparrow\uparrow$, $\downarrow\downarrow$, and $\uparrow\downarrow$ contributions, such that $v_c = v_c^{\uparrow\uparrow} + v_c^{\downarrow\downarrow} + v_c^{\uparrow\downarrow}$. These spin-resolved components of $v_c$ are important ingredients for the study and construction of dynamical exchange-correlation potentials in the spin channel.[16,17] They can be written as the expectation value of the Coulomb potential $1/r$ on the spin-resolved $g^c_{\sigma\sigma'}$,

$$v_c^{\sigma\sigma'}(r_s, \zeta) = \frac{(2 - \delta_{\sigma\sigma'})}{\sqrt{2}\, r_s} \frac{n_\sigma n_{\sigma'}}{n^2} \int_0^\infty g^c_{\sigma\sigma'}(x, r_s, \zeta)\, dx. \tag{73}$$

We have evaluated the r.h.s. of Eq. (73) by numerical integration of our QMC data for $g^c_{\sigma\sigma'}(x, r_s, \zeta)$, at

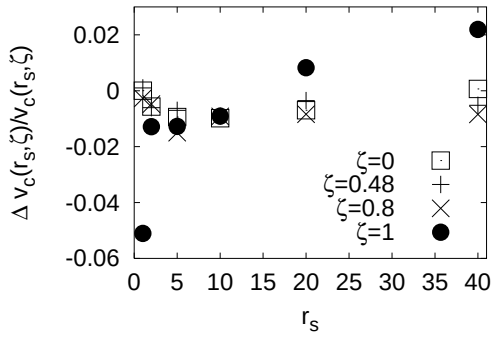



FIG. 8: Relative error $\Delta v_c(r_s,\zeta)/v_c(r_s,\zeta) = (v_c - v_c^{\rm INT})/v_c$ between $v_c$ calculated using the r.h.s. of Eq. (18) (with $\epsilon_c$ from Ref. 5), and $v_c^{\rm INT}$, obtained by numerical integration of $g^c$ (see text).

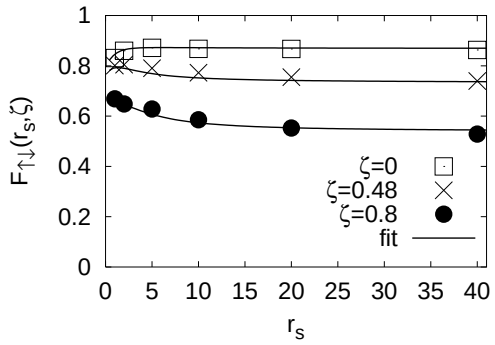



FIG. 9: Fraction of $\uparrow\downarrow$ contribution to the correlation part of the potential energy, $F_{\uparrow\downarrow} = v_c^{\uparrow\downarrow}/v_c$.

$\zeta = 0, 0.48, 0.8$, and $r_s = 1, 2, 5, 10, 20, 40$. This means that the integration in the r.h.s. of Eq. (73) has been truncated at $L/2$, where $L$ is the side of the simulation cell (in our case $L/2 \sim 6\, r_s$). The resulting $v_c^{\sigma\sigma'}$ are thus affected by the finite-size error, since they correspond to systems with fixed number of particles (see Sec. III) and an infinite-size extrapolation is not available in this case. One can get an idea of the magnitude of such error by using the same numerical-integration procedure for the spin-summed $g^c$, and then comparing the results with the corresponding thermodynamic limit, the last term of Eq. (18), combined with our[5] $\epsilon_c(r_s,\zeta)$. The relative error between the two evaluations of $v_c$ is reported in Fig. 8: it is of the order of few percents. At $\zeta = 1$, Figure 8 disproofs Eq. (10) of Ref. 8, which predicts a different virial theorem for the fully polarized system.

We have parametrized our spin-resolved $v_c^{\sigma\sigma'}(r_s,\zeta)$ as[41]

$$v_c^{\sigma\sigma'}(r_s,\zeta) = F_{\sigma\sigma'}(r_s,\zeta)\, v_c(r_s,\zeta). \tag{74}$$

The fractions $F_{\sigma\sigma}(r_s,\zeta)$ for parallel spins are well represented by

$$F_{\uparrow\uparrow}(r_s,\zeta) = F_{\uparrow\uparrow}^{\rm HD}(\zeta) + \left[w_1(\zeta)\, r_s + w_2(\zeta)\, r_s^2\right] \times \times \log\left(1 + \frac{w_3(\zeta)}{r_s^2}\right), \tag{75}$$

where the high-density $F_{\uparrow\uparrow}^{\rm HD}$ is given by Seidl,[42]

$$F_{\uparrow\uparrow}^{\rm HD}(\zeta) = \frac{-19.54\,(1+\zeta)}{153.38\mathcal{F}(\zeta) - 192.46}, \tag{76}$$

$$\mathcal{F}(\zeta) = \frac{(1+\zeta)\log(1+\zeta) + (1-\zeta)\log(1-\zeta)}{2\log(2)} + +0.0636\,\zeta^2 - 0.1024\,\zeta^4 + 0.0389\,\zeta^6, \tag{77}$$

and the functions $w_i(\zeta)$ have been obtained by fitting our data for $v_c^{\uparrow\uparrow}(r_s,\zeta)$ for $\zeta = -0.8, -0.48, 0., 0.48, 0.8$ (the negative $\zeta$ values corresponding to the $\downarrow\downarrow$ data),

$$w_1(\zeta) = (1-\zeta)\,(-0.006 - 0.03\,\zeta) \tag{78}$$

$$w_2(\zeta) = (1-\zeta)\,(-0.01 + 0.03\,\zeta) \tag{79}$$

$$w_3(\zeta) = 3.6\,(1+\zeta)^4. \tag{80}$$

Equations (75)-(80) completely determine the spin resolution of $v_c(r_s,\zeta)$, since $F_{\downarrow\downarrow}(r_s,\zeta) = F_{\uparrow\uparrow}(r_s,-\zeta)$ and $F_{\uparrow\downarrow} = 1 - F_{\uparrow\uparrow} - F_{\downarrow\downarrow}$.

In Fig. 9 we show our numerical results for the antiparallel-spin fraction $F_{\uparrow\downarrow}(r_s,\zeta)$, together with our fitting function; the relative errors on the fit of $v_c^{\uparrow\downarrow}$ (not shown) are of the same order of magnitude of those of Fig. 8. We see that the correlation part of the potential energy is completely dominated by the $\uparrow\downarrow$ contribution, even for $\zeta$ as high as 0.8.

**Acknowledgments**

We thank R. Asgari, S. De Palo, Z. Qian, S. V. Kravchenko, C. Tanguy, G. Vignale, and W. Yang for useful discussions, and gratefully acknowledge financial support from the Italian Ministry of Education, University and Research (MIUR) through COFIN 2003-2004 and the allocation of computer resources from INFM Iniziativa Calcolo Parallelo.

## APPENDIX A: LONG-RANGE SCALING

In this appendix we describe the construction of the long-range part of our $g^c$. We follow the same procedure used for the 3D case in Ref. 38, where the interested reader can find more details and comments on the relevant physics. Here we briefly recall the main equations and emphasize the differences between the 3D and the 2D case. As for the 3D case,[14] the results of this appendix can be used in the construction of a generalized-gradient approximation for a 2D correlation energy functional.

Following Ref. 38, we seek a scaling law for the long-range part of $g^c$. We call "long-range" part the

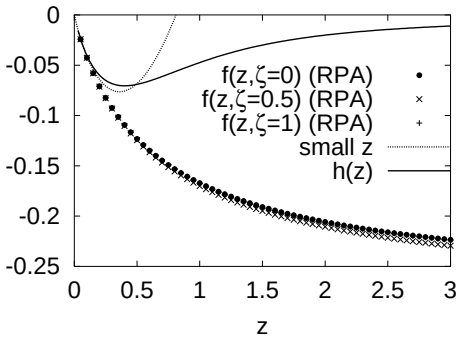



FIG. 10: The function $f(z,\zeta)$ [see Eq. (A1)], evaluated within RPA, for three different values of the spin polarization parameter $\zeta$. Also shown: the exact small-$z$ behavior of Eq. (A3) and the function $h(z)$ of Eq. (A8).

oscillation-averaged asymptotic behavior of $g^c$ for large $x = k_{\rm F} r$, or equivalently, the behavior of $S^c$ for small $q = k/k_{\rm F}$. From Eq. (15), we see that such a scaling law has the form

$$S^c(q \to 0, r_s, \zeta) \to \sqrt{2}\, r_s\, \phi^3\, f(z,\zeta), \qquad \text{(A1)}$$

where

$$z = \frac{k}{k_{TF}\phi^2} = \frac{q}{\phi^2\sqrt{2}\, r_s}, \qquad \text{(A2)}$$

is a variable on the scale of the Thomas-Fermi wavevector, $k_{TF}$ (which does not depend on $r_s$ in the 2D case), and the function $f(z,\zeta)$ has the small-$z$ expansion (independent of $\zeta$)

$$f(z \to 0, \zeta) = -\tfrac{2}{\pi} z + \tfrac{1}{\sqrt{2}} z^{3/2} + O(z^2). \qquad \text{(A3)}$$

The random-phase approximation (RPA) exactly recovers Eqs. (A1)-(A3). As in the 3D case,[38] we can thus obtain the function $f(z,\zeta)$ from RPA. Its (wrong) short-range behavior will be quenched in our parametrization of $g^c$ by the cutoff function $F_{\rm cut}(x)$ of Eq. (24).

We thus evaluated the function $f(z,\zeta)$ via the standard RPA equation

$$S^c_{\rm RPA}(q, r_s, \zeta) = -\int_0^\infty d\omega \frac{(\beta_\uparrow + \beta_\downarrow)^2}{q k_{\rm F}/\pi - (\beta_\uparrow + \beta_\downarrow)}, \qquad \text{(A4)}$$

with

$$\beta(q,\omega) = -\frac{2}{\pi q}\left[\frac{q}{2} - {\rm Re}\left(\sqrt{\left(\frac{q}{2} + i\frac{\omega}{q}\right)^2 - 1}\right)\right], \qquad \text{(A5)}$$

and

$$\beta_\uparrow = \beta\left(\frac{q}{\sqrt{1+\zeta}}, \frac{\omega}{1+\zeta}\right), \qquad \beta_\downarrow = \beta\left(\frac{q}{\sqrt{1-\zeta}}, \frac{\omega}{1-\zeta}\right). \qquad \text{(A6)}$$

The resulting $f(z,\zeta)$ has the small-$z$ expansion of Eq. (A3), and for large $z$ is equal to

$$f(z \to \infty, \zeta) = A(\zeta) + \frac{B(\zeta)}{z} + ... \qquad \text{(A7)}$$

Equation (A7) corresponds, in real space, to a divergent short-range behavior. As in three dimensions,[38] with a suitable cutoff Eq. (A7) recovers the RPA high-density expansion of the correlation energy, $\epsilon_c^{\rm RPA}(r_s \to 0, \zeta) = a_{\rm RPA}(\zeta) + b_{\rm RPA}(\zeta) r_s \log r_s + O(r_s)$. However, unlike the 3D case, in two dimensions the RPA correlation energy is not exact even in the $r_s \to 0$ limit.[37] Thus, while in three dimensions[20,21,38] the large-$z$ behavior of $f(z,\zeta)$ was important to recover the exact high-density limit of $\epsilon_c$, there is no need in 2D to keep Eq. (A7) in our parametrization. Moreover, as in three dimensions,[38] we find that the $\zeta$ dependence of $f(z,\zeta)$ is very weak (see Fig. 10), so that we can replace $f(z,\zeta)$ with $f(z,0)$ [this is exact in the "important" part of $f$, i.e., the small-$z$ regime of Eq. (A3)]. We thus define the function $h(z)$

$$h(z) = f(z,0) - A(0) - \frac{B(0)}{\sqrt{z^2 + [B(0)/A(0)]^2}} \qquad \text{(A8)}$$

where $A(0) = -0.272076$ and $B(0) = 10/\pi - 3$ correspond to the large-$z$ expansion for $\zeta = 0$ of Eq. (A7). As shown in Fig. 10, the function $h(z)$ has the same small-$z$ behavior of $f(z,\zeta)$, but goes to zero when $z \to \infty$, which corresponds to a less diverging short-range part in real space. The Fourier transform of $h(z)$ defines the function $f_1(v)$ of Eq. (25),

$$\frac{f_1(v)}{v} = \int_0^\infty h(z)\, z\, J_0(vz)\, dz, \qquad \text{(A9)}$$

where $v = \sqrt{2} r_s \phi^2 x$ is the appropriate real-space scaled variable. The function $f_1(v)$ has been evaluated numerically, and then parametrized as

$$f_1(v) = \frac{b_1\, v^{1/2} + b_2\, v + b_3\, v^{3/2} + b_4\, v^2 + b_5\, v^{5/2} + b_6\, v^3}{(v^2 + b_0^2)^{5/2}} \qquad \text{(A10)}$$

with

$$b_6 = 2/\pi \qquad \text{(A11)}$$

$$b_5 = -\frac{9}{4\pi}\frac{1}{\sqrt{2}}\left[\Gamma\left(\frac{3}{4}\right)\right]^2 \qquad \text{(A12)}$$

$$b_4 = -3\, b_0\left[\frac{b_1}{2 b_0^{5/2}}{\rm B}\left(\frac{3}{4},\frac{7}{4}\right) + \frac{b_2}{3 b_0^2} + \frac{b_3}{2 b_0^{3/2}}{\rm B}\left(\frac{5}{4},\frac{5}{4}\right) + \frac{b_5}{2 b_0^{1/2}}{\rm B}\left(\frac{3}{4},\frac{7}{4}\right) + \frac{2}{3} b_6\right], \qquad \text{(A13)}$$

$$b_3 = -22 \qquad b_2 = 61 \qquad b_1 = -64 \qquad b_0 = 3.46\,.$$

Eqs. (A11)-(A13) guarantee that the Fourier transform of $f_1(v)/v$ satisfies Eq. (A3). $\Gamma(x)$ and ${\rm B}(x,y)$ are the standard Gamma and Beta functions:[43] $\Gamma(3/4) \approx 1.225416702$, ${\rm B}(3/4, 7/4) \approx 0.8472130848$, ${\rm B}(5/4, 5/4) \approx 0.6180248924$.

## APPENDIX B: SPIN-RESOLUTION OF THE LONG-RANGE PART ($\zeta = 0$)

The long-range part of $g^c_{\sigma\sigma'}(x, r_s, \zeta = 0)$ has been simply approximated with Eq. (58), where the function $\tilde{f}_1(v, \alpha)$ is obtained from $f_1(v)$ of Eq. (A10) by replacing $b_6$ with $\tilde{b}_6 = 2(1/\pi + \alpha)$, and consequently changing $b_4$ according to Eq. (A13). In this way, the corresponding $S^c_{\sigma\sigma'}(q, r_s, \zeta = 0)$ exactly recovers Eq. (56).


[1] see e.g. T. Ando, A. B. Fowler, and F. Stern, Rev. Mod. Phys. **54**, 437 (1982); E. Abrahams, S. V. Kravchenko M. P. Sarachik, Rev. Mod. Phys. **73**, 251 (2001).

[2] S. V. Kravchenko and M. P. Sarachik, Rep. Prog. Phys. **67**, 1 (2004).

[3] E. Abrahams, P. W. Anderson, D. C. Licciardello, and T. V. Ramakrishnan, Phys. Rev. Lett. **42**, 673 (1979)

[4] S.M. Reimann and M. Manninen, Rev. Mod. Phys. **74**, 1283 (2002).

[5] C. Attaccalite, S. Moroni, P. Gori-Giorgi, and G.B. Bachelet, Phys. Rev. Lett. **88** 256601 (2002); **91**, 109902(E) (2003).

[6] see e.g., A.A. Shashkin, M. Rahimi, S. Anissimova, S.V. Kravchenko, V. T. Dolgopolov, and T. M. Klapwijk, Phys. Rev. Lett. **91**, 046403 (2003); O. Prus, Y. Yaish, M. Reznikov, U. Sivan, and V. Pudalov, Phys. Rev. B **67**, 205407 (2003); I.A. Shelykh, N.T. Bagraev, and L.E. Klyachkin, Phys. Solid State **45**, 2189 (2003).

[7] J. Zhu, H.L. Störmer, L.N. Pfeiffer, K.W. Baldwin, and K.W. West, Phys. Rev. Lett. **90**, 056805 (2003).

[8] J. Moreno, and D.C. Marinescu, Phys. Rev. B **68**, 195210 (2003).

[9] K. Kärkkäinen, M. Koskinen, S. M. Reimann, and M. Manninen, Phys. Rev. B **68**, 205322 (2003); E. Räsänen *et al.*, Phys. Rev. B **67**, 235307 (2003). Phys. Rev. B **67**, 235307 (2003).

[10] see, e.g., H. Saarikoski, E. Räsänen, S. Siljamäki, A. Harju, M.J. Puska, and R.M. Nieminen, Phys. Rev. B **67**, 205327 (2003); H. Jiang, H.U. Baranger, and W. Yang Phys. Rev. B **68**, 165337 (2003).

[11] D.J.W. Geldart and D. Neilson, Phys. Rev. B **67**, 045310 (2003).

[12] M. Vogt, R. Zimmermann and R. J. Needs, Phys. Rev. B **69**, 045113 (2004).

[13] S. De Palo, M. Botti, G. Senatore, and S. Moroni, in preparation.

[14] J.P. Perdew, in *Electronic Structure of Solids '91*, edited by P. Ziesche and H. Eschrig (Akademie Verlag, Berlin 1991); J.P. Perdew, K. Burke, and Y. Wang, Phys. Rev. B **54**, 16533 (1996).

[15] O. Gunnarsson, M. Jonson, and B. I. Lundqvist, Phys. Lett. A **59**, 177 (1976); Phys. Rev. B **20**, 3136 (1979).

[16] Z. Qian and G. Vignale, Phys. Rev. B **68**, 195113 (2003).

[17] Z. Qian, submitted to Phys. Rev. B

[18] A. K. Rajagopal, J. C. Kimball, and M. Banerjee, Phys. Rev. B **18**, 2339 (1978); X.-Y. Pan and V. Sahni, J. Chem. Phys. **119**, 7083 (2003).

[19] D. Pines and P. Nozières, *Theory of Quantum Liquids* (Benjamin, New York, 1966).

[20] J. P. Perdew and Y. Wang, Phys. Rev. B **46**, 12947 (1992); **56**, 7018(E) (1997).

[21] P. Gori-Giorgi and J.P. Perdew, Phys. Rev. B **66**, 165118 (2002).

[22] N.H. March, Phys. Rev. **110**, 604 (1958); P.N. Argyres, Phys. Rev. **154**, 410 (1967); N. Iwamoto, Phys. Rev. B **38**, 4277 (1988); L. Kleinman, Phys. Rev. B. **43**, 3918 (1991).

[23] S. Baroni and S. Moroni, Phys. Rev. Lett. **82**, 4745 (1999).

[24] For a recent review, see W. M. C. Foulkes, L. Mitas, R. J. Needs and G. Rajagopal, Rev. Mod. Phys. **73** 33 (2001).

[25] B. Tanatar and D. M. Ceperley, Phys. Rev. B **39**, 5005 (1989).

[26] F. Rapisarda and G. Senatore, Aust. J. Phys. **49**, 161 (1996).

[27] Y. Kwon, D. M. Ceperley, and R. M. Martin, Phys. Rev. B **58**, 6800 (1998).

[28] G. Ortiz and P. Ballone, Phys. Rev. B **50**, 1391 (1994)

[29] Y. Kwon, D. M. Ceperley, and R. M. Martin, Phys. Rev. B **53**, 7376 (1996).

[30] For the low-density limit, we have simply fitted the frequency and phase of our oscillating term to a model pair-distribution function built from gaussian orbitals centered on the sites of a triangular lattice. In the present work we are dealing with the fluid state, not with the crystal, and the *damping* of the oscillations is completely different in the two cases. But the *position* of the maxima, which is practically the same in the fluid and crystalline state, is the only information which we extract from this model.

[31] P. Gori-Giorgi, F. Sacchetti, and G.B. Bachelet, Phys. Rev. B **61**, 7353 (2000); **66**, 159901(E) (2002).

[32] G.B. Bachelet, P. Gori-Giorgi, and F. Sacchetti, AIP Conf. Proc. **577**, 21 (2001).

[33] G.S. Atwal and N.W. Ashcroft, Phys. Rev. B **67**, 233104 (2003).

[34] G.S. Atwal, I.G. Khalil, and N.W. Ashcroft, Phys. Rev. B **67**, 115107 (2003).

[35] M. Lein, E.K.U. Gross, and J.P. Perdew, Phys. Rev. B **61**, 13431 (2000).

[36] R. Asgari, M. Polini, B. Davoudi, M. P. Tosi, Phys. Rev. B **68**, 235116 (2003).

[37] A.K. Rajagopal and J.C. Kimball , Phys. Rev. B **15**, 2819 (1977).

[38] Y. Wang and J. P. Perdew, Phys. Rev. B **44**, 13298 (1991).

[39] M. Polini, G. Sica, B. Davoudi, and M.P. Tosi, J. Phys.: Condens. Matter **13**, 3591 (2001).

[40] P. Gori-Giorgi and J.P. Perdew, Phys. Rev. B **64**, 155102 (2001).

[41] P. Gori-Giorgi and J.P. Perdew, Phys. Rev. B **69**, 041103(R) (2004).

[42] M. Seidl, cond-mat/0312146.

[43] M. Abramowitz and I. Stegun, *Handbook of Mathematical Functions* (Dover Publications Inc., New York, 1965).